Atomic-resolution transmission electron microscopy of electron beam–sensitive crystalline materials

Atomic-resolution transmission electron microscopy of electron beam-sensitive crystalline materials

Daliang Zhang,[1*] Yihan Zhu,[2⊥] Lingmei Liu,[2] Xiangrong Ying,[2] Chia-En Hsiung,[2] Rachid Sougrat,[1] Kun Li,[1*] and Yu Han[2,3*]

[1] King Abdullah University of Science and Technology (KAUST), Imaging and Characterization Core Lab, Thuwal 23955-6900, Saudi Arabia.

[2] King Abdullah University of Science and Technology (KAUST), Advanced Membranes and Porous Materials Center, Physical Sciences and Engineering Division, Thuwal 23955-6900, Saudi Arabia.

[3] King Abdullah University of Science and Technology (KAUST), KAUST Catalysis Center, Physical Sciences and Engineering Division, Thuwal 23955-6900, Saudi Arabia.

[⊥] Current address: Department of Chemical Engineering, Zhejiang University of Technology, Hangzhou 310014, China PR.

*Corresponding author. Email: daliang.zhang@kaust.edu.sa; kun.li@kaust.edu.sa; yu.han@kaust.edu.sa

Abstract: High-resolution imaging of electron beam-sensitive materials is one of the most difficult applications of transmission electron microscopy (TEM). The challenges are manifold, including the acquisition of images with extremely low beam doses, the time-constrained search for crystal zone axes, the precise image alignment, and the accurate determination of the defocus value. We develop a suite of methods to fulfill these requirements and acquire atomic-resolution TEM images of several metal organic frameworks that are generally recognized as highly sensitive to electron beams. The high image resolution allows us to identify individual metal atomic columns, various types of surface termination, and benzene rings in the organic linkers. We also apply our methods to other electron beam-sensitive materials, including the organic-inorganic hybrid perovskite $CH_3NH_3PbBr_3$.

One Sentence Summary: We describe a suite of methods for high-resolution transmission electron microscopy imaging of beam-sensitive materials.

Main Text: Understanding the fundamental structure-property relationships in functional materials is the essence of materials science. High-resolution TEM (HRTEM) is a powerful tool for structure characterization (*1*). However, there are a wide range of materials that are easily damaged by the electron beams (*2-5*). Metal organic frameworks (MOFs), which have designable porous structures and fascinating properties (*6-8*), represent a typical example of electron beam-sensitive materials. During the few attempts to image MOFs using HRTEM, only the primary channels could be resolved by the limited resolution as a result of beam damage (*2, 9-11*).

The mechanisms of beam damage are complex and vary with the material, primarily including knock-on damage, heating effects, and radiolysis (*3, 4, 12*). One means of alleviating beam damage is to reduce the energy of electron beam. HRTEM with low accelerating voltages has successfully imaged carbon nanotube and graphene (*13-15*). However, the use of low-energy electrons results in poor image resolution and a short penetration depth, and only prevents knock-on damage. Similarly, the use of cryo-TEM only lessens the heating damage to a certain degree (*11*). An alternative, in-principle more general solution to this issue is to acquire the HRTEM images with a sufficiently low electron dose to capture the structure before damage occurs. Although this idea is straightforward, it is difficult to realize because it requires an extremely sensitive camera to record acceptable images with only a few electrons per pixel. Conventional cameras cannot produce images with a sufficient signal-to-noise ratio under such low dose conditions.

Direct-detection electron-counting (DDEC) cameras have an unprecedentedly high detective quantum efficiency and enable HRTEM at ultralow electron doses (*16*, *17*). Taking advantage of this, structural biologists have boosted the voxel resolution for protein structures using cryo-TEM (*18*). In the field of materials science, however, the potential of DDEC cameras in HRTEM imaging of electron beam-sensitive materials remains largely unexplored, due to some practical obstacles. First, unlike the single-particle cryo-TEM that reconstructs a protein structure from randomly oriented particles, for crystalline materials images should be acquired along specific directions, i.e., along the zone axes of the lattice. With beam-sensitive specimens, the process of finding a zone axis must be accomplished very quickly to minimize the beam irradiation. Second, the electron-counting mode is capable of producing successive short-exposure images, but the images must be precisely aligned to fully restore the high resolution information. Third, it is impossible to acquire a focus series of a beam-sensitive material, even when using a DDEC camera,

and thus the interpretation of the image is difficult unless an accurate defocus value can be determined. We reported the use of a DDEC camera to image a MOF material (ZIF-8) with an ultralow electron dose, in which the zone-axis image was obtained by sampling a large number of randomly oriented crystals (*19*). However, this is an inefficient trial-and-error process and success is not guaranteed. In this work, we develop a suite of methods to overcome these obstacles, advancing the HRTEM of beam-sensitive materials to a nearly routine process.

To design the quantitative HRTEM conditions for MOFs, we first evaluated their stabilities under a 300 KV-accelerated electron beam. The results reveal they began to lose their crystallinity when the cumulative electron dose reached 10-20 $e^- Å^{-2}$, as determined by the fading of the electron diffraction (ED) spots (fig. S1). These values set the upper limits of the cumulative electron dose for both locating a zone axis and the subsequent image acquisition. In our experiments, we used a DDEC camera to acquire images at a reasonably high magnification of 55,000 to achieve atomic resolution (pixel size: 0.57 Å × 0.57 Å) with electron doses of 2-4 e^- per pixel (6-12 $e^- Å^{-2}$). Therefore, the maximum electron dose that can be used to find a zone axis is less than 10 $e^- Å^{-2}$. The conventional, manual method for aligning a zone axis does not meet this threshold, because it requires time-consuming, iterative toggles between the diffraction and imaging modes, often causing the total electron dose to reach hundreds of electrons per $Å^2$.

We developed a simple program to achieve a direct, one-step alignment of the zone axis (figs. S2 and S3). When the electron beam incidence deviates from a zone axis by an angle φ, the zero-order Laue zone of the lattice intersects with the Ewald sphere, forming an arc in the ED that is part of the Laue circle. The radius of the Laue circle is approximately equal to $\sin(\varphi)*(1/\lambda)$, where λ is the wavelength of the beam. Our program first identifies a Laue circle by analyzing the distribution of reflections from an off-axis ED pattern. Different from an earlier software of automatic zone axis alignment (*20*) that estimates the crystal orientation by evaluating the intensities of reflections, our program determines the Laue circle from the positions of reflections to avoid the influence of structure factors or dynamic effects. Once the Laue circle is identified, φ is determined by its radius and λ. The program then decomposes φ into two components, φ_α and φ_β, which correspond to two tilting angles around the α-tilt and β-tilt axes of the double-tilt TEM holder, based on the predetermined directions of the two tilting axes. By applying the program-calculated tilting angles φ_α and φ_β, we can directly tilt the crystal from the initial orientation to

align with the zone axis. The whole process requires the acquisition of only two EDs, one for determining the Laue circle and the other for confirming the on-axis orientation; the electron beam is blanked in between while the program does its calculations, and the total dose consumed is far below 1 $e^-/Å^2$. This method requires that the initial crystal orientation is close to a zone axis ($-5^\circ < \varphi < 5^\circ$); otherwise, there are very few reflections observed in ED, making the identification of a Laue circle difficult. In practice, the probability of seeing a Laue circle is > 10% in randomly oriented powder samples.

HRTEM of electron beam-sensitive materials often suffers from a beam-induced specimen motion that results in blurred images. When using a DDEC camera, this issue can be overcome by breaking the total exposure into a stack of successive short-exposure images (frames), on the condition that the drift between frames can be precisely corrected by image alignment. In principle, the exposure of each frame should be as short as possible to minimize specimen motion and statistical errors from the detector. However, beam-sensitive materials require low electron dose rate to avoid structural damage, and consequently, short exposure times result in very noisy frames with poor signal to noise that cannot be aligned using the common methods based on feature matching or phase correlation. To increase the signal to noise, several successive frames can be merged into one, which is equal to using longer exposure and thus detrimental to image resolution, especially when the specimen motion is severe. Image filters can also increase the signal to noise to facilitate image alignment, but the existing filters do not work well with high noise levels (fig. S4).

A general principle of image alignment is to decompose a real-space image into components of different spatial frequencies in the reciprocal space by Fourier transform (FT). Image drift can be determined from the 'phases' variation in the FTs. The difficulty in aligning noisy images lies in the poor signal to noise that affects the accuracy of phase determination. We hypothesize that the impact of noise can be minimized by selectively analyzing pixels in the FT with strong amplitudes, because phase determination of weak pixels is more easily influenced by noise and prone to errors. On the basis of this hypothesis, we developed an "amplitude filter" to confine the phase analysis to 'reliable' strong-amplitude pixels (figs. S5 and S6).

Unlike the common methods that deal with the weak signals of individual frames, the "amplitude filter" starts by integrating the FTs of all the frames in an image stack to pinpoint the

strong-amplitude pixels. The workflow is illustrated in **Fig. 1** using an HRTEM image stack of MOF UiO-66 (*21*). With extremely low dose (0.033 e^-/pixel) (**Fig. 1A**), even the reflections are difficult to identify in the FT of each frame (**Fig. 1B**). We summed the FT amplitude components from all of the frames in the stack, as the reflections have invariable coordinates in the FTs, irrespective of image drift. As shown in **Fig. 1C**, the "hidden" reflections emerged in the summed FT amplitude pattern (we call it 'amplitude pattern' because it does not contain phase information). We filtered out background and weak pixels that have amplitudes lower than a set threshold from the amplitude pattern. The "amplitudes" of the remaining pixels were combined with the "phases" from the original FT of each frame to generate a series of modified FTs (**Fig. 1D**), followed by inverse FTs to generate a series of filtered images (**Fig. 1E**). Finally, the image drift was calculated using iterative cross-correlation based on the filtered images (**Fig. 1F**), and this information was used to align the original images in the stack. The drift-corrected, summed image shows rich high-resolution structural details, as evidenced by the appearance of the 1.4 Å reflection in the FT (**Fig. 1G**). By contrast, the cross-correlation without our "amplitude filter" could not correctly align this image stack until it is 1×1×10 binned, which led to a marked reduction in image resolution in the direction of the image drift (**Fig. 1H**). The result of merging all of the frames without drift correction is shown in **Fig. 1I** for comparison.

We are now able to study various MOFs with TEM along different zone axes, and to restore high-resolution information from the obtained images. Results from MOF UiO-66 are presented in **Fig. 2**. The successful acquisition of HRTEM images from four zone axes, <001>, <011>, <111>, and <013>, demonstrates the effectiveness of our method for zone axis alignment. FTs of these images show that the information transfer is < 2 Å in all directions (**Fig. 2**), confirming the efficacy of our method for image alignment.

The contrast in HRTEM images varies with the specimen thickness and defocus, making a single image difficult to interpret directly. A common practice in HRTEM is to acquire a series of images with different defocuses for structure reconstruction (*22, 23*). But this method is not suitable for MOFs because it is impossible to acquire multiple images without causing structural damage, even when using the low-dose conditions. On the other hand, the very low framework density of MOFs greatly decreases their effective scattering thickness; therefore, we can safely apply the weak-phase object approximation to MOFs for a wide range of thicknesses up to ~ 100

nm. Therefore, a single image can be made more interpretable by correcting the "contrast inversion" caused by the contrast transfer function (CTF) of the objective lens, if the absolute defocus of the image is known (*24*). Here we propose that we can take advantage of the "instability" of MOFs to determine the defocus. Specifically, after an HRTEM image is captured, we prolong the beam irradiation to deliberately destroy the crystalline structure, and acquire a focus series of this amorphized area (fig. S7). Using established methods (*22*), we can determine the absolute defocus value of each image in the series and, thus, that of the HRTEM image of MOF for CTF correction.

The success of our methodology has been demonstrated in a case study, in which an HRTEM image of UiO-66 along the <011> axis was acquired, aligned, and CTF-corrected using the methods described above. The sample was heated at 300 °C under vacuum for 10 h to remove the solvent/guest molecules before HRTEM. The imaged area contains a truncated octahedral crystal with an ultra-thin piece of crystal protruding from its lower right corner (**Fig. 3A**). In the CTF-corrected and denoised image (**Fig. 3B** and fig. S8), triangular channels encompassed by three metal clusters and three 1,4-benzenedicarboxylic acids (BDC) are identified, and atomic columns of Zr are distinguished within the Zr_6O_8 clusters, in good agreement with the crystal structure of UiO-66. The benzene rings with face-on configurations in the BDC linkers are resolved (**Fig. 3B** and fig. S8). In addition to the bulk structure, our image reveals detailed local structures. At the truncation surface of the octahedral crystal that corresponds to the fast-growing {100} planes, the crystal growth steps are identified as a number of small {100} and {111} facets (**Fig. 3C**). Furthermore, the high resolution allows us to investigate the surface termination of this crystal. In the CTF-corrected image, the outermost layer of Zr clusters have dark contrast and can be identified at the crystal surfaces, where the organic linkers are hardly visible because of the weak contrast associated with the low atomic numbers. We performed real-space averaging along the crystal surface to enhance the signal to noise (fig. S9). The results reveal the coexistence of ligand-free (metal-exposing) and ligand-capped surfaces: the major exposed {111} surface terminates with BDC linkers (**Fig. 3D**); in contrast, the small truncation surface (growth steps) expose Zr clusters at the kink positions between {100} and {111} facets (**Fig. 3E**).

It has been speculated that upon heating to 300 °C, the octahedral $ZrO_4(OH)_4$ clusters in UiO-66 undergo dehydroxylation forming distorted Zr_6O_6 clusters (*25*). In a <110> projection, this distortion gives rise to increased Zr-Zr distances along the in-plane <110> direction (fig. S10).

However, the random orientation of this distortion makes it difficult to verify by conventional characterizations. Using HRTEM, we observed the subtle structural change in UiO-66 associated with dehydroxylation (figs. S11 to S13). As revealed in the images, the as-synthesized UiO-66 contains only one type of Zr cluster with uniform Zr-Zr distances of 3.34 Å, whereas the heated UiO-66 contains two types of Zr clusters; one is same as the cluster in the as-synthesized sample and the other has larger Zr-Zr distances of 3.89 Å (**Fig. 3, F and G**, and fig. S12). This result supports speculation that the Zr clusters in UiO-66 become distorted upon heating (*25*). The appearance of a small number of undistorted clusters (Zr-Zr: 3.34 Å) in the heated UiO-66 (fig. S13) was likely caused by partial re-hydroxylation during the TEM sample preparation process. We note that the exact values of the Zr-Zr distance measured using HRTEM are not very accurate due to the pixel size limitations.

HRTEM images of MOFs ZIF-8 and HKUST-1 (*26*) and a germanosilicate zeolite are presented in figs. S14 and S15, which show good matching with the corresponding crystal structures after CTF-correction. We also successfully acquired HRTEM images of the organic-inorganic hybrid perovskite $CH_3NH_3PbBr_3$, which has emerged as an optoelectronic material and is known to be very sensitive to electron beams. The hybrid perovskites show anomalous I-V hysteresis in photovoltaic applications (*27*). Ferroelectric effect (*28*) and ion migration (*29*) have been posited to be likely causes for the hysteresis. Our image reveals that $CH_3NH_3PbBr_3$ crystals contain ordered nanometer-sized domains with off-centered CH_3NH_3 cations that have differing orientations. In the two typical domains highlighted in **Fig. 4**, the CH_3NH_3 cations exhibit normal and parallel configurations (relative to the projection direction), giving rise to in-plane and out-of-plane electric dipoles, respectively. This observation implies the ferroelectric order in this material.

In summary, we developed a suite of methodologies that enable atomic-resolution TEM imaging of electron beam-sensitive crystalline materials, which have traditionally been considered unsuitable for TEM characterization. With this capability, we are able to observe the local structures of MOFs and other fragile materials, significantly expanding the range of applications for HRTEM. It is worth noting that our method for zone axis alignment not only reduces the electron dose, but also enhances the precision of alignment. Its application is not limited to beam-sensitive materials; it is particularly useful for aligning nanosized crystals. Likewise, our method

for image alignment can be generally applied to various noisy images with periodic features. This study facilitates investigations in a wide variety of "unstable" materials using HRTEM.

References and Notes

1. C. L. Jia, M. Lentzen, K. Urban, Atomic-resolution imaging of oxygen in perovskite ceramics. *Science* **299**, 870-873 (2003).
2. J. Cravillon *et al.*, Rapid Room-Temperature Synthesis and Characterization of Nanocrystals of a Prototypical Zeolitic Imidazolate Framework. *Chem. Mater.* **21**, 1410-1412 (2009).
3. O. Ugurlu *et al.*, Radiolysis to knock-on damage transition in zeolites under electron beam irradiation. *Phys. Rev. B* **83**, (2011).
4. T. Susi *et al.*, Atomistic Description of Electron Beam Damage in Nitrogen-Doped Graphene and Single-Walled Carbon Nanotubes. *ACS Nano* **6**, 8837-8846 (2012).
5. A. Garcia *et al.*, Analysis of electron beam damage of exfoliated MoS(2) sheets and quantitative HAADF-STEM imaging. *Ultramicroscopy* **146**, 33-38 (2014).
6. H. Li, M. Eddaoudi, M. O'Keeffe, O. M. Yaghi, Design and synthesis of an exceptionally stable and highly porous metal-organic framework. *Nature* **402**, 276-279 (1999).
7. H. Furukawa, K. E. Cordova, M. O'Keeffe, O. M. Yaghi, The chemistry and applications of metal-organic frameworks. *Science* **341**, 1230444 (2013).
8. O. K. Farha *et al.*, De novo synthesis of a metal-organic framework material featuring ultrahigh surface area and gas storage capacities. *Nat. Chem.* **2**, 944-948 (2010).
9. O. I. Lebedev, F. Millange, C. Serre, G. Van Tendeloo, G. Ferey, First direct imaging of giant pores of the metal-organic framework MIL-101. *Chem. Mater.* **17**, 6525-6527 (2005).
10. L. K. Zhu, D. L. Zhang, M. Xue, H. Li, S. L. Qiu, Direct observations of the MOF (UiO-66) structure by transmission electron microscopy. *CrystEngComm* **15**, 9356-9359 (2013).
11. C. Wiktor, S. Turner, D. Zacher, R. A. Fischer, G. Van Tendeloo, Imaging of intact MOF-5 nanocrystals by advanced TEM at liquid nitrogen temperature. *Micropor. Mesopor. Mat.* **162**, 131-135 (2012).
12. R. F. Egerton, Mechanisms of radiation damage in beam-sensitive specimens, for TEM accelerating voltages between 10 and 300 kV. *Microsc. Res. Tech.* **75**, 1550-1556 (2012).
13. A. Hashimoto, K. Suenaga, A. Gloter, K. Urita, S. Iijima, Direct evidence for atomic defects in graphene layers. *Nature* **430**, 870-873 (2004).
14. J. C. Meyer *et al.*, Experimental analysis of charge redistribution due to chemical bonding by high-resolution transmission electron microscopy. *Nat. Mater.* **10**, 209-215 (2011).
15. L. H. Guan, K. Suenaga, S. Iijima, Smallest carbon nanotube assigned with atomic resolution accuracy. *Nano Lett.* **8**, 459-462 (2008).
16. L. Jin *et al.*, Applications of direct detection device in transmission electron microscopy. *J. Struct. Biol.* **161**, 352-358 (2008).

17. X. M. Li *et al.*, Electron counting and beam-induced motion correction enable near-atomic-resolution single-particle cryo-EM. *Nat. Methods.* **10**, 584-590 (2013).

18. A. Merk *et al.*, Breaking Cryo-EM Resolution Barriers to Facilitate Drug Discovery. *Cell* **165**, 1698-1707 (2016).

19. Y. Zhu *et al.*, Unravelling surface and interfacial structures of a metal-organic framework by transmission electron microscopy. *Nat. Mater.* **16**, 532-536 (2017).

20. T. Duden, A. Gautam, U. Dahmen, KSpaceNavigator as a tool for computer-assisted sample tilting in high-resolution imaging, tomography and defect analysis. *Ultramicroscopy* **111**, 1574-1580 (2011).

21. J. H. Cavka *et al.*, A new zirconium inorganic building brick forming metal organic frameworks with exceptional stability. *J. Am. Chem. Soc.* **130**, 13850-13851 (2008).

22. W. Wan, S. Hovmoller, X. D. Zou, Structure projection reconstruction from through-focus series of high-resolution transmission electron microscopy images. *Ultramicroscopy* **115**, 50-60 (2012).

23. H. W. Zandbergen, D. Tang, J. Jansen, R. J. Cava, The use of through focus exit wave reconstruction in the structure determination of several intermetallic superconductors. *Ultramicroscopy* **64**, 231-247 (1996).

24. X. D. Zou, S. Hovmöller, P. Oleynikov, *Electron Crystallography: Electron Microscopy and Electron Diffraction*. (Oxford University Press, 2011), pp. 177-190.

25. L. Valenzano *et al.*, Disclosing the Complex Structure of UiO-66 Metal Organic Framework: A Synergic Combination of Experiment and Theory. *Chem. Mater.* **23**, 1700-1718 (2011).

26. S. S. Chui, S. M. Lo, J. P. Charmant, A. G. Orpen, I. D. Williams, A chemically functionalizable nanoporous material. *Science* **283**, 1148-1150 (1999).

27. H. J. Snaith *et al.*, Anomalous Hysteresis in Perovskite Solar Cells. *J. Phys. Chem. Lett.* **5**, 1511-1515 (2014).

28. J. Wei *et al.*, Hysteresis Analysis Based on the Ferroelectric Effect in Hybrid Perovskite Solar Cells. *J. Phys. Chem. Lett.* **5**, 3937-3945 (2014).

29. W. Tress *et al.*, Understanding the rate-dependent J-V hysteresis, slow time component, and aging in CH3NH3PbI3 perovskite solar cells: the role of a compensated electric field. *Energy Environ. Sci.* **8**, 995-1004 (2015).

30. F. Brivio, K. T. Butler, A. Walsh, M. van Schilfgaarde, Relativistic quasiparticle self-consistent electronic structure of hybrid halide perovskite photovoltaic absorbers. *Phys. Rev. B* **89**, (2014).

31. Z. D. Xu, L. Z. Yang, C. L. Xu, Pt@UiO-66 Heterostructures for Highly Selective Detection of Hydrogen Peroxide with an Extended Linear Range. *Anal. Chem.* **87**, 3438-3444 (2015).

32. N. L. Torad *et al.*, Facile synthesis of nanoporous carbons with controlled particle sizes by direct carbonization of monodispersed ZIF-8 crystals. *Chem. Comm.* **49**, 2521-2523 (2013).

33. F. L. Wang, H. L. Guo, Y. M. Chai, Y. P. Li, C. G. Liu, The controlled regulation of morphology and size of HKUST-1 by "coordination modulation method". *Micropor. Mesopor. Mat.* **173**, 181-188 (2013).

34. W. J. Roth *et al.*, A family of zeolites with controlled pore size prepared using a top-down method. *Nat. Chem.* **5**, 628-633 (2013).

35. J. A. Sichert *et al.*, Quantum Size Effect in Organometal Halide Perovskite Nanoplatelets. *Nano Lett.* **15**, 6521-6527 (2015).

36. W. Wan, J. Sun, J. Su, S. Hovmoller, X. Zou, Three-dimensional rotation electron diffraction: software RED for automated data collection and data processing. *J. Appl. Crystallogr.* **46**, 1863-1873 (2013).

37. QSTEM V2.31 (http://www.qstem.org).

38. M. V. Sidorov, ctfExplorer V0.999a (http://www.maxsidorov.com/ctfexplorer).

39. R. Kilaas, Optimal and near-optimal filters in high-resolution electron microscopy. *J. Microsc-Oxford* **190**, 45-51 (1998).

40. D. R. G. Mitchell, HRTEM filter V1.3 (https://www.felmi-zfe.at/dm-script/dm-script-database/).

41. X. Liu *et al.*, Isomorphous Incorporation of Tin Ions into Germanosilicate Framework Assisted by Local Structural Rearrangement. *ACS Catal.* **6**, 8420-8431 (2016).

Acknowledgments: We thank M. Pan and O. Terasaki for helpful discussions. This work was supported by King Abdullah University of Science and Technology through Competitive Research Grant (URF/1/2570-01) and Center Competitive Funding (FCC/1/1972-19). HRTEM images presented in this paper and the two programs used for zone axis alignment and image alignment are archived in a data repository (https://zenodo.org/record/1133206) for verification purposes only. Interested readers can download the programs after agreeing with the terms and conditions stated there. D. Z., Y. Z., K. L., and Y. H. are inventors on United States Provisional patent applications (62/490,967 and 62/490,968) submitted by King Abdullah University of Science and Technology that cover the methods for crystal zone axis alignment and image alignment.

Supplementary Materials:

Materials and Methods

Figures S1-S16

Table S1

References (*31-41*)

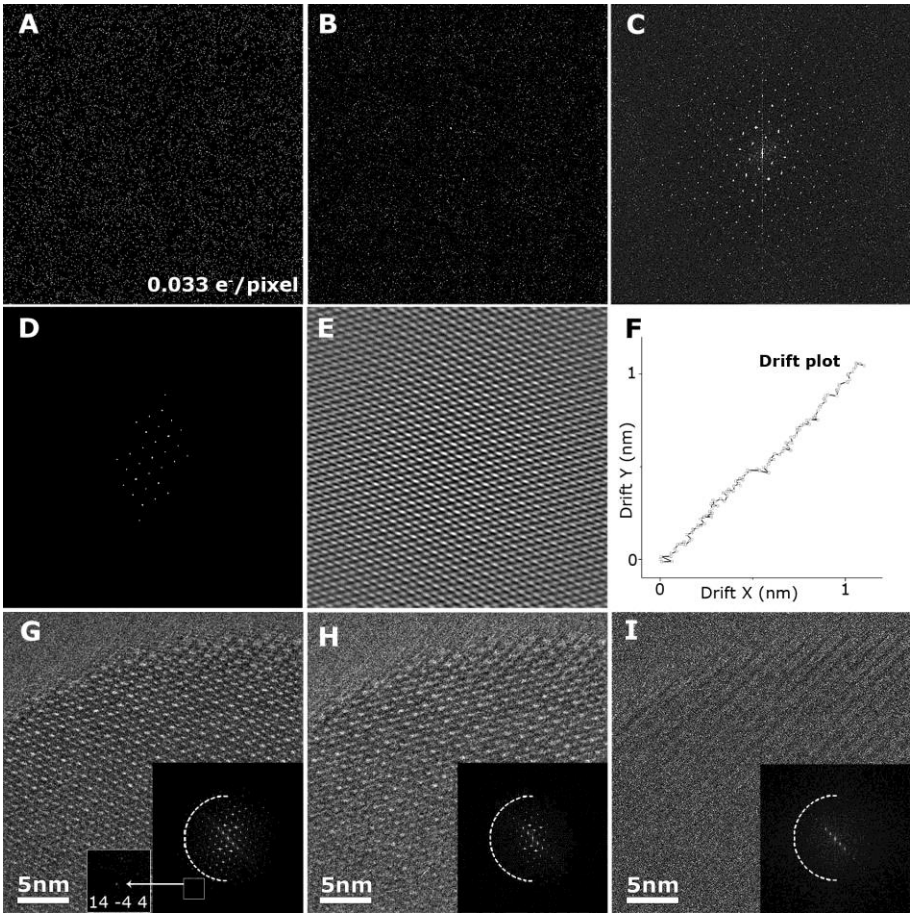

Fig. 1. Alignment of an image stack using the "amplitude filter". (**A**) A single frame and (**B**) the corresponding FT in an HRTEM image stack (120 frames in total) acquired for UiO-66 along the <011> zone axis. (**C**) The FT amplitude pattern formed by summing up the FT amplitude component of all frames. (**D**) Modified FT of a single frame by adopting filtered amplitudes from (C). (**E**) An amplitude-filtered single frame that is produced by inverse FT of (D). (**F**) The image-drift profile determined from filtered frames. (**G**) The drift-corrected image based on (F). (**H**) The drift-corrected image by cross-correlation, where the image stack is 1×1×10 binned to enhance the signal to noise. (**I**) Uncorrected image formed by directly summing up all the frames. In (G)-(I), the corresponding FTs are shown as insets; the half circles represent the frequency of 2 Å. In (G), a local area is zoomed in to highlight the observed 14 -4 4 reflection (d = 1.4 Å).

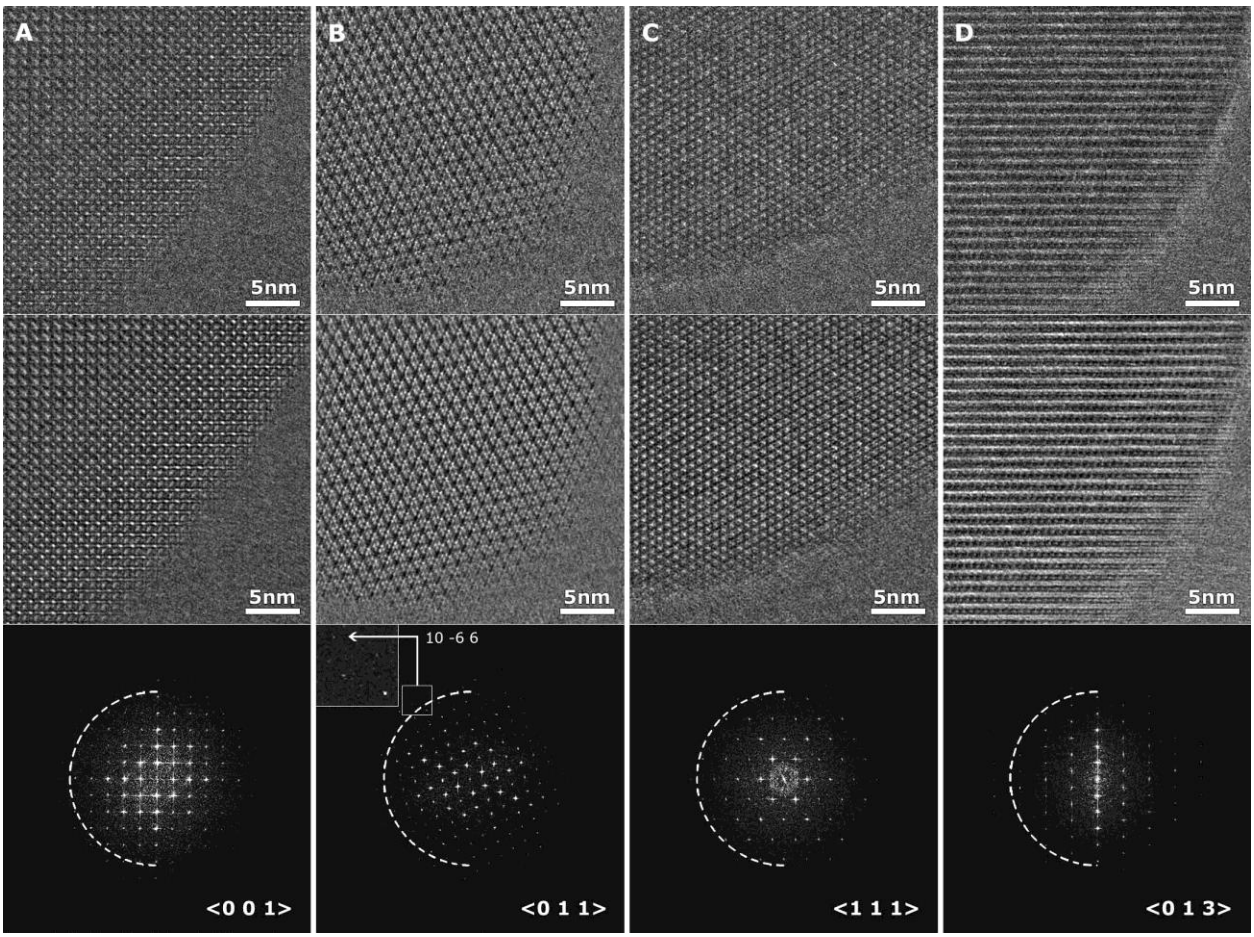

Fig. 2. HRTEM images of UiO-66 acquired from different zone axes: (**A**) <001>, (**B**) <011>, (**C**) <111> and (**D**) <013>. The top, middle, and bottom rows show raw images, denoised images and FTs of the raw images, respectively. The half circles in the FTs represent 2 Å. In all directions, there are reflections observed beyond the circle, indicating that the information transfer is less than 2 Å. As an example, the 10 -6 6 reflection (d = 1.6 Å) is highlighted in (B).

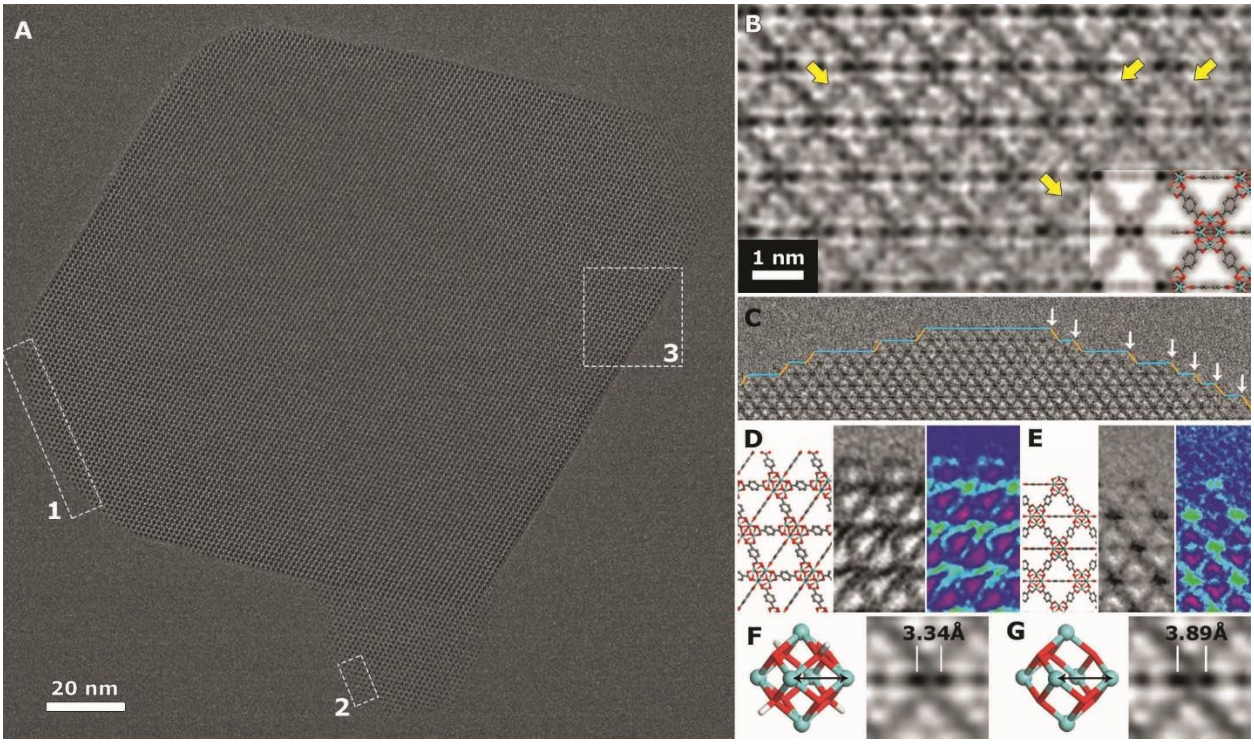

Fig. 3. HRTEM of thermally treated UiO-66. (**A**) Drift-corrected HRTEM image of a truncated octahedral UiO-66 crystal and an ultra-thin piece of crystal with the same <011> orientation. (**B**) CTF-corrected denoised image from the ultra-thin crystal (area 2 in (A)), showing triangular channels, individual Zr atomic columns, and the BDC linkers. The benzene rings in the BDC linkers are indicated by the arrows. Overlays are simulated projected potential maps and a projected structural model of UiO-66 for comparison. (**C**) A truncation surface (area 1 in (A)), showing crystal growth steps involving small {100} facets and {111} facets (labeled in blue and yellow, respectively). The white arrows indicate "kink" positions between {100} and {111} facets. (**D**) Ligand-terminated {111} surface: (left) structural model; (middle) processed HRTEM image by real-space averaging of 5 motifs from area 3 in (A); (right) the averaged image displayed in the rainbow colors to increase the visibility of the ligand contrast. (**E**) Ligand-free (metal-terminated) {100}/{111} kink: (left) structural model; (middle) processed HRTEM image by real-space averaging of 7 motifs from area 1 in (A); (right) the averaged image displayed in the rainbow colors. (**F** and **G**) The structure model (left) and the processed HRTEM image (right) of the (F) hydroxylated and (G) dehydroxylated Zr clusters featuring different Zr-Zr distances. The image processing details are shown in fig. S13.

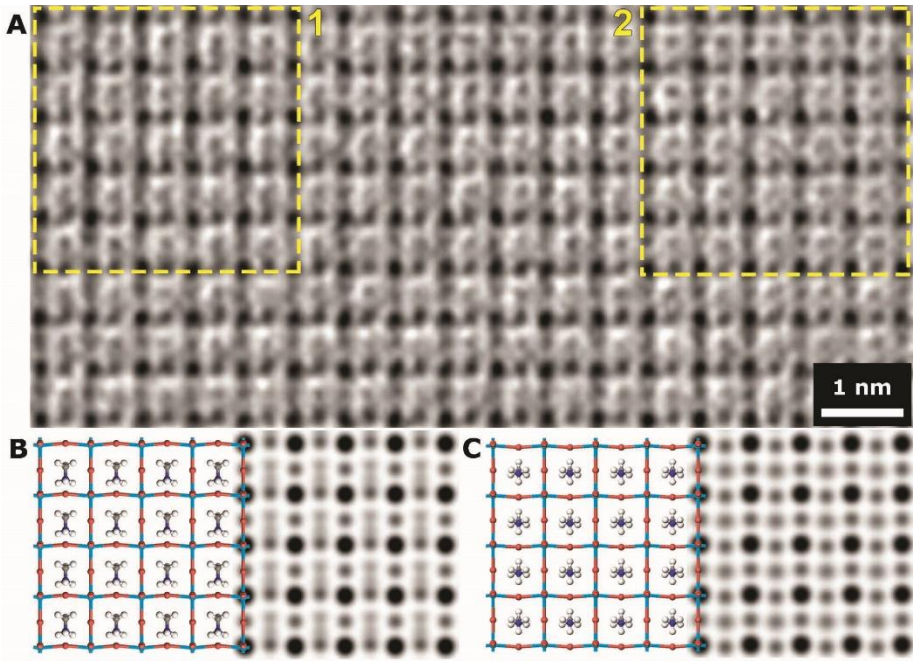

Fig. 4. HRTEM of organic-inorganic hybrid perovskite $CH_3NH_3PbBr_3$. (**A**) CTF-corrected denoised HRTEM image. The raw image is shown in fig. S16. The squares highlight two ordered domains with off-centered CH_3NH_3 cations that have differing orientations. (**B** and **C**) The structural model (left) (*30*) and the simulated projected potential map (right) of $CH_3NH_3PbBr_3$ with different CH_3NH_3 orientations, corresponding to region 1 and 2 in (A), respectively. In (B) and (C), the off-centered CH_3NH_3 cations exhibit normal and parallel configurations (relative to the projection direction), giving rise to in-plane and out-of-plane electric dipoles, respectively.